# JGR Oceans

## Influence of Stratification and Yucatan Current Transport on the Loop Current Eddy Shedding Process

Efraín Moreles[1,2] , Jorge Zavala-Hidalgo[2] , Benjamín Martínez-López[2] , and Angel Ruiz-Angulo[3]

[1]Instituto de Ciencias del Mar y Limnología, Unidad Académica Procesos Oceánicos y Costeros, Universidad Nacional Autónoma de México, Mexico City, Coyoacán, Mexico, [2]Centro de Ciencias de la Atmósfera, Universidad Nacional Autónoma de México, Mexico City, Coyoacán, Mexico, [3]Icelandic Meteorological Office, Reykjavík, Iceland

**Abstract** The effects of stratification and Yucatan Current (YC) transport on the dynamics of the Loop Current (LC) and Loop Current Eddies (LCEs) are studied using a primitive equation, 2½ nonhomogeneous layered model, which reproduces the main dynamical features of the upper ocean circulation in the Gulf of Mexico (GoM). The analysis considers the observed variations in stratification and YC transport, and their expected changes due to climate change. The study is based on a set of long-term simulations considering the combination of seven stratification configurations with seven transport configurations resulting in 49 cases. The LCE shedding period and diameter (LCE metrics) and kinetic energy, eddy kinetic energy, available potential energy, eddy available potential energy, and the energy Burger number (energy metrics) are analyzed. The stratification and transport contribute to the current and future LC and LCE variability, with their dynamics being more sensitive to transport variations than to stratification variations. The LCE detachment is associated with the increase in the mass of the LC and its available potential energy budget, which is a primary determinant for the LC and LCE dynamics and a condition for eddy shedding. For the expected changes due to climate change, the LCE response is contrary: larger stratification causes increments in the LCE metrics and energy metrics, except the energy Burger number that decreases; conversely, smaller transport causes the opposite response. A combined occurrence of increased stratification and reduced transport, as expected with climate change, causes decrements in the LCE metrics and energy in the GoM.

**Plain Language Summary** To understand the changes in the physical, chemical, biological, and economic processes that occur in the Gulf of Mexico (GoM) is necessary to study its ocean circulation. The Loop Current (LC) and the large eddies that detach from it, called Loop Current Eddies (LCEs), have been recognized as major components of the GoM circulation. Here we used a computational model of intermediate complexity to study the influence of stratification and transport of the Yucatan Current (YC) on the LC and LCEs, considering the current and future conditions under climate change. The future conditions, based on climate change scenarios, consider increased stratification and reduced YC transport. We found that stratification and YC transport significantly affect the LC and LCE behavior, but transport variations are dominant. The dynamics of the LCEs is highly correlated with the increase in the mass of the LC and its available potential energy budget. For the expected changes due to climate change, the LCE response is contrary: larger stratification causes increments in the shedding period and diameter of LCEs; conversely, smaller YC transport causes the opposite response. A combined occurrence of increased stratification and reduced YC transport causes decrements in the shedding period and diameter of LCEs.

## 1. Introduction

The Loop Current System (LCS), composed by the Loop Current (LC) and the Loop Current Eddies (LCEs), constitutes the main circulation pattern and source of variability in the Gulf of Mexico (GoM; NASEM, 2018). The LCS plays a key role in the region by determining its climate and weather (Oey et al., 2005; Schmitz et al., 2005), and by affecting all the economic activities in the region (Yoskowitz et al., 2013). The LC originates in the Yucatan Channel as the Yucatan Current (YC), where it enters the GoM forming an anticyclonic-looping circulation before turning east and exiting through the Florida Straits, becoming the Florida Current and then the Gulf Stream (NASEM, 2018). The LC develops in a continuum of stages between the retracted and extended stages. In the retracted stage, the LC enters the GoM and turns east to

exit through the Florida Straits. In the extended stage, the LC penetrates northward with a mean northward speed between 16.5 and 26.4 km·month$^{-1}$, reaching approximately 28°N, where it episodically sheds large anticyclonic eddies (the LCEs) with diameters ranging from 200 to 300 km, at intervals of 3–17 months. The LCEs move westward at a speed of approximately 2–5 km·day$^{-1}$, exchanging mass, momentum, and dissolved matter between them and the water masses in the western GoM (Leben, 2005; NASEM, 2018; Oey et al., 2005; Schmitz et al., 2005).

The dynamics of the LCS has been a topic of great interest for the scientific community since its first studies till the present (Donohue et al., 2016; Hamilton et al., 2019; Leipper, 1970; Reid, 1972), particularly the mechanisms of formation and shedding of the LCEs. Several mechanisms involved in the LCS dynamics have been studied, for examples: zonal momentum conservation of the LC flow (Nof, 2005; Pichevin & Nof, 1997), potential vorticity conservation (Reid, 1972), structure of the transport of the YC (Athié et al., 2015; Bunge et al., 2002; Chang & Oey, 2012, 2013; Hurlburt & Thompson, 1980; Lin et al., 2009; Oey et al., 2003; Sheinbaum et al., 2002), LC frontal eddies (Le Hénaff et al., 2012; Schmitz, 2005; Zavala-Hidalgo et al., 2003), LC penetration blocked by cyclones (Zavala-Hidalgo et al., 2006), wind stress over the GoM (Chang & Oey, 2010; Oey et al., 2003), vorticity flux through the Yucatan Channel (Candela et al, 2002, 2003; Oey, 2004), Caribbean eddies that squeeze through the Yucatan Channel (Murphy et al., 1999; Zavala-Hidalgo et al., 2003; Athiée et al., 2012), anchoring of the LC by the west Florida shelf (Weisberg & Liu, 2017), and deep eddies and bottom baroclinic instability (Chéerubin et al., 2005; Donohue et al., 2016; Hamilton et al., 2016; Yang et al., 2020; Maslo et al., 2020). Despite all the research carried out concerning the dynamical mechanisms of the LCS, to date there is no complete understanding of it (NASEM, 2018).

The structure of the YC transport is a key process that determines the LCS dynamics. Using numerical models, Oey et al. (2003), Lin et al. (2009), and Chang and Oey (2012, 2013) found that the YC transport is minimum when the LC has a strong intrusion into the GoM, just before a LCE shedding may occur. After the shedding, the transport increases during the growth phase of the LC. Nevertheless, questions remain about the effects of variations in the YC transport on the LCS dynamics.

Recently, appreciable changes in the ocean due to climate change that can modify the dynamics of the LCEs have been documented. Rhein et al. (2014) observed warming and increased thermal stratification of the upper ocean of about 4% in the first 200 m depth for the period 1971–2010, which is expected to continue and strengthen during the 21st century. Liu et al. (2012) studied the possible impact of anthropogenic global warming on the GoM using a high resolution version of the Miami Isopycnic Coordinate Ocean Model under the IPCC-A1B scenario and found a reduction in the volume transport of the YC of 20% (from 24 Sv to 19 Sv) by the late 21st century. The extent to which the structure of stratification modifies the LCE shedding process has not been studied, and the effect of the YC transport variations on the eddy shedding process has been hardly addressed.

This work aims to study the variability of the LCE shedding process due to thermal stratification and YC transport. Additionally, the expected variations in the eddy shedding process due to climate change, which are increased upper stratification (Rhein et al., 2014) and reduced YC transport (Liu et al., 2012), are analyzed. For these objectives, a simple isopycnal layered model that reproduces the main characteristics of the LCE shedding process was chosen to isolate the effect of these mechanisms on its dynamics.

## 2. Methods

This section describes the model used, the design of the numerical experiments, and the methods to study the LCE shedding process.

### 2.1. Numerical Model

Of particular interest to this study is the fact that a simple reduced gravity model can reproduce, in a realistic way, the main characteristics of the LCE shedding process (Hurlburt & Thompson, 1982). Thus, a model of this type represents a simple but valuable tool to obtain a deep understanding of different mechanisms affecting the eddy shedding processes in an isolated manner and reveal causal relationships associated with the mechanisms considered. Isopycnal layered models remain as valuable tools to study various ocean
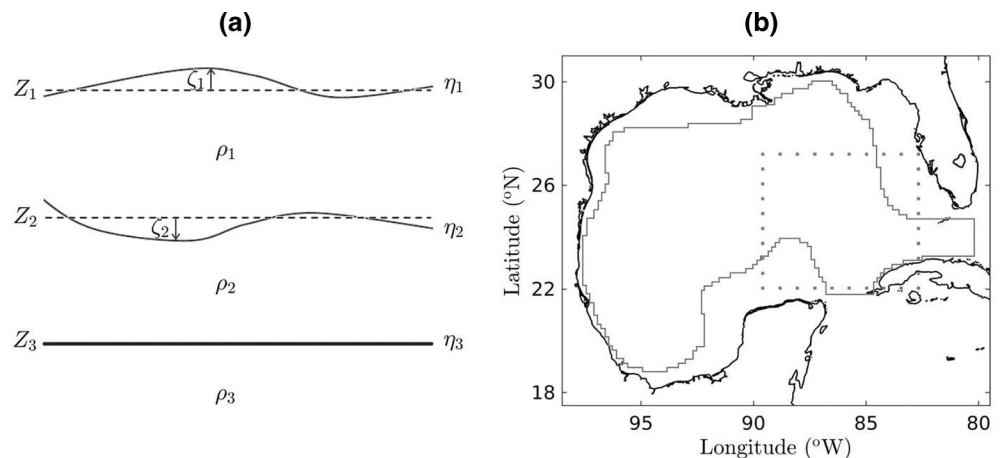
**Figure 1.** (a) Schematic representation of the vertical structure of the model. For each layer $k$, $\rho_k$ are the densities, $Z_k$ are the constant heights of the interfaces of a reference state at rest, $\zeta_k$ are the vertical displacements of the layer boundaries, and $\eta_k = Z_k + \zeta_k$ are the interfaces. Image adapted from Colin de Verdière et al. (2018). (b) The horizontal domain of the model used to simulate the dynamics of the Gulf of Mexico, approximately delimited by the 200 m depth contour (gray line). The dotted line box specifies the intrusion region of the Loop Current ([89.59°W, 82.67°W] × (22.04°N, 27.20°N]). Image adapted from Zavala-Hidalgo (1997).

phenomena worldwide (e.g., McCreary & Lu, 1994; Peterson & Greatbatch, 2001; Simonnet et al., 2003; Zhao et al., 2020).

The model selected for this study is based on the model developed by Zavala-Hidalgo (1997), which is a 2½ nonhomogeneous layered model that solves the primitive equations for the ocean. The model used reproduces the main dynamical features of the upper circulation in the GoM, including the penetration-retraction of the LC, the shedding and westward translation of LCEs, the large anticyclonic gyre in the northwestern GoM, the cyclonic gyre in the Bay of Campeche, as well as the processes of entrainment-detrainment, advection, and surface heat fluxes (Zavala-Hidalgo, 1997; Zavala-Hidalgo et al., 2002).

The model has three layers: an active upper layer representing the mixed layer (Niiler & Kraus, 1977), an active intermediate layer, and an infinite-depth motionless, deep layer (Figure 1a). Exchanges of heat, momentum, and mass are allowed through the interfaces, as well as entrainment-detrainment between the upper and intermediate layers. The model domain is restricted to the ocean region deeper than 200 m, with such depth contour as the lateral boundary, and it does not include bottom topography (Figure 1b). At the open boundaries (the Yucatan Channel and the Florida Straits), the boundary conditions are specified by imposing flows in geostrophic balance, an inflow at the Yucatan Channel and an outflow at the Florida Straits; whereas in the rigid boundary, the no-slip condition is prescribed on the tangential flow. The model cannot represent the mass flow between the continental shelf and deep zones, LC-shelf-slope interactions, bottom friction effects, deep processes, and the generation of topographic Rossby waves due to the collision of the LCEs against the western continental slope of the GoM.

In this study, heat and momentum fluxes between the upper layer and the atmosphere were shut off to separate the LCE response between oceanic and atmospheric forcings and provide results only due to ocean processes. In this model, for a given configuration, the LCS behavior is very regular, that is, the temporal variability of the episodes of intrusion-retraction of the LC an eddy shedding is small. The features of the model fulfill the requirements for this study since it can be estimated with very high confidence the changes in the LCE shedding process due to specific configurations and forcings. The model focuses on representing upper ocean processes and changes in the LCS due to variations in the open boundary conditions to help understand the effects of stratification and YC transport. The model is not intended to reproduce the entire structure of the GoM circulation due to all processes involved in its dynamics, nor to deliver an entirely realistic representation of the GoM hydrodynamics. If the intention were to have a model that included the greatest number of processes that affect the LCS variability, another model would have been chosen, but for the objectives of this study, the 2½ layered model has great advantages.

**Table 1**
*Physical Parameters for the Base Configuration of the Model Used to Simulate the Dynamical Processes of This Study.*
$\langle H_1 \rangle_{\text{ref}}$ *and* $\langle H_2 \rangle_{\text{ref}}$ *Denote the Temporal Mean of the Area Integral of the Thickness of the Upper and Intermediate Layers, Respectively*

| | | |
|---|---|---|
| Transport through the upper layer | $\Upsilon_{1(\text{ref})}$ | 5.6 Sv |
| Transport through the intermediate layer | $\Upsilon_{2(\text{ref})}$ | 16.5 Sv |
| Transport of the Yucatan Current above the 12.0°C isotherm | $\Upsilon_{\text{ref}} = \Upsilon_{1(\text{ref})} + \Upsilon_{2(\text{ref})}$ | 22.1 Sv |
| Temperature of the upper layer | $T_1$ | 27.0°C |
| Temperature of the intermediate layer | $T_2$ | 15.0°C |
| Temperature of the bottom layer | $T_3$ | 4.0°C |
| Mean thickness of the upper layer | $\overline{\langle H_1 \rangle}_{\text{ref}}$ | 76 m |
| Mean thickness of the intermediate layer | $\overline{\langle H_2 \rangle}_{\text{ref}}$ | 422 m |

*Note.* Other unspecified parameters as those used by Zavala-Hidalgo (1997) and Zavala-Hidalgo et al. (2002).

A base configuration of the model was implemented, similar to the current average conditions of the LCS. From this configuration, the stratification and YC transport were varied to study the LCE shedding process. The base configuration does not consider exchanges between the intermediate and deep layers. The values of thickness and temperature in each active layer were chosen in accordance with observations of the vertical thermal structure in the Yucatan Channel (Candela et al., 2019; Sheinbaum et al., 2002). The upper layer is located between the sea surface and the 25.0°C isotherm, with a fixed temperature of 27.0°C and a mean thickness of 76 m. The intermediate layer is located between the 25.0°C and 12.0°C isotherms, with a fixed temperature of 15.0°C and a mean thickness of 422 m. For the bottom layer, the temperature was set to a fixed value of 4.0°C.

The transport for each active layer was chosen in accordance with observations of the transport across the Yucatan Channel, which indicate high variability in its average value. Sheinbaum et al. (2002) used instrumented moorings and measured a mean YC transport of 23.8 Sv during the period between September 1999 and June 2000. Rousset and Beal (2010, 2011) used 5 years of velocity data from May 2001 to May 2006 and quantified a transport of 30.3 Sv across the Yucatan Channel and of 30.8 Sv across the Florida Straits. Athié et al. (2015) used current observations from a mooring array and obtained a mean YC transport of 26.1 Sv from May 2010 to June 2013. Candela et al. (2019) estimated an average transport of 27.6 Sv across the Yucatan Channel and the Florida Straits using instrumented moorings from September 2012 to August 2016. The vertical profile of the YC transport per unit depth obtained by Rousset and Beal (2010, 2011), in combination with the results of Sheinbaum et al. (2002), Athié et al. (2015), and Candela et al. (2019), were used as a reference to specify the imposed transport for each active layer in the model: 5.6 Sv for the upper layer and 16.5 Sv for the intermediate layer, resulting in a transport of 22.1 Sv above the 12.0°C isotherm.

The physical parameters used for the base configuration are shown in Table 1, with other unspecified parameters as those used by Zavala-Hidalgo (1997) and Zavala-Hidalgo et al. (2002). Throughout the study, the following notation is used. The mean temporal value of any function $f(\vec{x}, t)$ over a certain time period is defined by $\overline{f(\vec{x})} \equiv \int f(\vec{x}, t) \, dt \, / \int dt$, with the corresponding fluctuation component expressed as $f'(\vec{x}, t) = f(\vec{x}, t) - \overline{f(\vec{x})}$. The area integral is denoted by $\langle f(t) \rangle \equiv \iint_A f(\vec{x}, t) \, dA$, with $dA$ being the area of each grid cell in the model domain.

The numerical model was solved using a C-grid and a leap-frog scheme for the temporal integration, with a zonal and meridional grid-size of 1/12° and a time-step of 300 s. The model was run from rest by inflow through the Yucatan Channel and integrated for 30 years. The outputs of the model were recorded every 10 days, with the results for the first 10 years taken as a spin-up and the remaining 20 years used for the analysis.
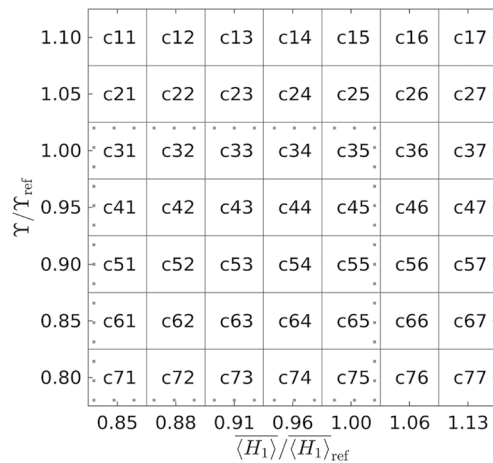
**Figure 2.** Diagram of the case studies simulated. Each case study is identified with a label, with the case c35 corresponding to the base configuration. The case studies for climate change are those delimited by the dotted line box. The upper layer thickness and Yucatan Current transport are represented by $\langle H_1 \rangle$ and $\Upsilon$, respectively, with the subscript 'ref' denoting the variables for the base configuration.

## 2.2. Numerical Experiments

This work aims to study the variability of the LCE shedding process related to variations in upper stratification and YC transport in the observed range, as well as the expected variations of these due to climate change. For this aim, a sensitivity analysis of the LCE shedding process was carried out, which considered different values of the upper layer thickness $\langle H_1 \rangle$ and YC transport $\Upsilon$ above the 12.0°C isotherm. The numerical experiments are described below, in which the upper layer thickness and YC transport for the base configuration are denoted with the subscript "ref".

Concerning stratification, monthly variations of the mixed layer depth over the GoM open waters from 18 m to 77 m have been measured (Damien et al., 2018). Additionally, climate change has been associated with an observed increment in the upper thermal stratification of 4% during the period 1971–2010, which is expected to continue (Liu et al., 2012). The variations in $\langle H_1 \rangle$ considered in this study range from 64.8 m to 86.2 m, representing changes of −15% to 13% with respect to $\overline{\langle H_1 \rangle}_{\text{ref}}$ (see Table 1). The variation range of $\langle H_1 \rangle$ is limited by the numerical computational behavior of the model.

The measured average YC transport shows variations of up to 6.5 Sv (Athié et al., 2015; Candela et al., 2019; Rousset & Beal, 2010, 2011; Sheinbaum et al., 2002), which represent variations of 27% with respect to its minimum observed value of 23.8 Sv. Projected estimates for this transport due to climate change indicate a 20% reduction by the end of the century (Rhein et al., 2014). In this study, variations in $\Upsilon$ from 17.7 Sv to 24.3 Sv were considered, representing changes of −20% to 10% with respect to $\Upsilon_{\text{ref}}$ (see Table 1).

The numerical experiments include the combination of seven values of $\langle H_1 \rangle$ with seven values of $\Upsilon$, for a total of 49 case studies (Figure 2). Each case study is referred to as a GoM configuration (a specific combination of stratification and YC transport). The corresponding temperature and density of the layers were kept constant throughout each case study; hence, a reduction in the upper layer thickness can be considered an increase in the upper stratification because the vertical variation of the density $\Delta\rho/\Delta z$ increased. For each case study, the transport in the upper and intermediate layers was scaled accordingly, and other parameters of the model (Table 1) were not changed.

From the base configuration case (case c35), the cases with larger stratification and smaller YC transport (the cases delimited by the dotted line box in Figure 2) can be regarded as those representing the climate change conditions, according to Rhein et al. (2014) and Liu et al. (2012).

## 2.3. LCE Shedding Process

### 2.3.1. Metrics for the LCS

The analysis of the LC is carried out through a continuous monitoring of it using a specific contour of the sea surface height (Hamilton et al., 2000). This contour serves as a proxy for the location of the LC, providing it matches the location of maximum gradients in sea surface topography and allows continuous monitoring of the LCEs during their westward translation. From this contour, the LC metrics can be calculated, which comprise its northernmost latitude $LC_{NL}$, westernmost longitude $LC_{WL}$, length $LC_L$, area $LC_A$, and circulation $LC_C$. The first four are referred to as the geometric metrics, whereas the circulation is referred to as a dynamical metric.

According to Hamilton et al. (2000), to identify a LCE shedding event the LC metrics should be plotted as time series, where each shedding event is associated with the local minimum in these time series after an extended intrusion of the LC. Then, the LCE metrics can be calculated, which comprise the shedding period $LCE_P$ and diameter $LCE_D$ of the LCEs as well as the LC retreat latitude $LC_{RL}$. Among all the LC metrics, the LC circulation exhibits the most regular behavior to identify a LCE shedding event (Hamilton et al., 2000).

In this work, the LC location was specified as a contour of the upper layer thickness satisfying the conditions specified by Hamilton et al. (2000). The LC and LCE metrics were computed from this contour and collectively referred to as the LCS metrics. Particularly, the LC circulation was calculated as the line integral of the velocity in the upper layer along the LC contour,

$$\mathrm{LC_C} = \oint \vec{v}_1 \cdot \vec{\mathrm{ds}} = \int u_1 \, \mathrm{d}x + \int v_1 \, \mathrm{d}y, \tag{1}$$

where $u_1$ and $v_1$ are the zonal and meridional velocity components, respectively, and $\mathrm{d}x$ and $\mathrm{d}y$ are the zonal and meridional grid-sizes, respectively.

### 2.3.2. Energy Analysis

The budget of available potential energy (APE) is an important element to study the formation of eddies and the energetics of ocean circulation (Gill et al., 1974; Lorenz, 1955; Reid et al., 1981). Mesoscale eddies are generated by baroclinic instability, deriving their energy from the APE of the large-scale mean circulation (Donohue et al., 2016; Gill et al., 1974). The APE of a fluid is the difference between the total potential energy of a given state and a reference state (one with minimum potential energy in which the isosteric and isobaric surfaces are level) obtained after an isentropic readjustment of the given state. It represents the maximum amount of total potential energy that can be converted into kinetic energy and be used to drive motions and form eddies (Lorenz, 1955; Reid et al., 1981).

There are several methodologies to estimate the APE. A suitable formulation is the one derived by Colin de Verdière et al. (2018) considering a shallow water system in isopycnic coordinates. For $n$ numbers of layers, the APE as a function of time $t$ and space in the horizontal plane $\vec{x}$ is given by

$$\mathrm{APE}(\vec{x},t) = g\rho_1 \frac{\zeta_1^2(\vec{x},t)}{2} + \sum_{k=2}^{n} g(\rho_k - \rho_{k-1})\frac{\zeta_k^2(\vec{x},t)}{2}, \tag{2}$$

where $g$ is the gravitational acceleration, $\rho_k$ is the density of the $k$th layer, and $\zeta_k$ is the vertical displacement of a fluid particle in layer $k$ at vertical position $Z_k$ in the reference state at time $t = 0$, which moves adiabatically to another vertical position $\eta_k$ at time $t$, $\eta_k = Z_k + \zeta_k$, staying on the same side of a density interface (Figure 1a).

Additionally, the horizontal kinetic energy (KE) can be used to study the energy of eddies, which can be expressed as (Colin de Verdière et al., 2018),

$$\mathrm{KE}(\vec{x},t) = \sum_{k=1}^{n} \rho_k H_k(\vec{x},t)\frac{\left|\vec{v}_k(\vec{x},t)\right|^2}{2}, \tag{3}$$

where for each $k$th layer, $H_k = \eta_k - \eta_{k+1}$ is the layer thickness and $\vec{v}_k = (u_k, v_k)$ is the horizontal velocity. Both the APE and KE are expressed in energy per unit area (J·m$^{-2}$). The APE and KE fields can be decomposed into their mean and eddy fields:

$$\mathrm{MAPE}(\vec{x}) = g\rho_1 \frac{\left[\overline{\zeta_1(\vec{x})}\right]^2}{2} + \sum_{k=2}^{n} g(\rho_k - \rho_{k-1})\frac{\left[\overline{\zeta_k(\vec{x})}\right]^2}{2}, \tag{4}$$

$$\mathrm{EAPE}(\vec{x}) = g\rho_1 \frac{\overline{\zeta_1'^2(\vec{x})}}{2} + \sum_{k=2}^{n} g(\rho_k - \rho_{k-1})\frac{\overline{\zeta_k'^2(\vec{x})}}{2}, \tag{5}$$

$$\mathrm{MKE}(\vec{x}) = \sum_{k=1}^{n} \rho_k \overline{H_k(\vec{x})}\frac{\left[\overline{u_k(\vec{x})}\right]^2 + \left[\overline{v_k(\vec{x})}\right]^2}{2}, \tag{6}$$

$$\mathrm{EKE}\left(\vec{x}\right) = \sum_{k=1}^{n}\rho_k \overline{H_k\left(\vec{x}\right)}\frac{\overline{u_k'^2\left(\vec{x}\right)} + \overline{v_k'^2\left(\vec{x}\right)}}{2}, \tag{7}$$

where MAPE is the mean available potential energy, EAPE is the eddy available potential energy, MKE is the mean kinetic energy, and EKE is the eddy kinetic energy.

The energy analysis considered the computation of the total energy fields and the energy Burger number over the LC intrusion region (the dotted box in Figure 1b). The total energy fields were computed as area integrals of the corresponding fields (Equations 4–7) and denoted by ⟨MAPE⟩, ⟨EAPE⟩, ⟨MKE⟩, and ⟨EKE⟩. The energy Burger number $Bu_e = ⟨\mathrm{MKE}⟩/⟨\mathrm{MAPE}⟩$ gives a measure of the LCS dynamics since it scales like the dynamical Burger number $Bu$, that is, $Bu_e \sim Bu = R_d^2 / L^2$, where $R_d$ is the first Rossby radius of deformation and $L$ is the horizontal length scale of the circulation (Gill et al., 1974). The total energy fields and the energy Burger number are collectively referred to as the energy metrics.

## 3. Results and Discussion

This section shows the results concerning the validation of the numerical model, the description of the LCE shedding process, the sensitivity of the LCE shedding process to varying stratification and YC transport, as well as its expected variations due to climate change. Additionally, it is presented a comparison of the results of this study with those of a theoretical one.

### 3.1. Validation of the Numerical Model

For the validation of the numerical model used, the base configuration results were analyzed and compared with observations and results obtained using oceanic general circulation models (OGCMs). The LCS and energy metrics, the spatial distribution pattern of the energy fields, and the LCE trajectories were also analyzed.

The mean values of the LCS metrics and the energy metrics for the base configuration are shown in Table 2. The mean values of the LCS metrics are consistent with those reported using observations (see e.g., Hall & Leben, 2016; Hamilton et al., 2000; Leben, 2005; Sturges & Leben, 2000; Vukovich, 2012). The mean LCE shedding period of 180 days coincides with the primary peak of the corresponding histogram estimated using observational databases (Hamilton et al., 2000; Leben, 2005; Sturges & Leben, 2000). The standard deviation of the LCS metrics is small compared to observations, which makes possible an in-depth analysis of changes in the LCS behavior due to varying stratification and YC transport. The energy Burger number ($Bu_e = 13.70 \times 10^{-4}$) is in the order of those resulting from global dynamics: $Bu_e = 16.80 \times 10^{-4}$ (Colin de Verdière et al., 2018), $Bu_e = 7.03 \times 10^{-4}$ (Zemskova et al., 2015), $Bu_e = 6.68 \times 10^{-4}$ (Oort et al., 1989), and $Bu_e \sim 10 \times 10^{-4}$ (Gill et al., 1974).

The spatial distribution pattern of the mean and eddy energy fields, given by Equations 4–7, is shown in Figure 3, which also includes the individual LCE trajectories (gray lines) and the mean LCE trajectory (red line) computed using the algorithm developed by Nencioli et al. (2010). The core of the LC and the core of the LCEs when they have reached the western GoM are zones with the highest MAPE values since they maintain vertical displacements of the isopycnal surfaces from a reference state through time (Figure 3a). EAPE describes the temporary variations in MAPE, so zones with high EAPE identify the formation region and trajectories of the LCEs, consistent with energy transfer from EAPE to EKE due to baroclinic instability (Donohue et al., 2016; Yang et al., 2020). Zones with high EAPE are mostly located in the eastern GoM deeper than 1,000 m (Figure 3b), consistent with Yang et al. (2020). The close relationship between the EAPE (Figure 3b) and EKE (Figure 3d) patterns is noticeable (cf. Colin de Verdière et al., 2018; Yang et al., 2020). EKE also describes the temporal variations of the mean velocity field. The region of variable penetration of the LC, the eastern side of the eddies when they have reached the western GoM, and the southern jet in the western boundary of the GoM are zones with high EKE (Figure 3d). The MKE field well describes the mean circulation, with zones with high values located in the LC region and the region with the regular presence of LCEs in the northwestern GoM (Figure 3c).

**Table 2**
*Values of the Loop Current System Metrics for the Base Configuration and From Observations; and Energy Metrics for the Base Configuration*

| Metric | This study | Hall and Leben (2016) |
|---|---|---|
| LCE shedding period | $\text{LCE}_P = 180\,\text{days}$ | $\text{LCE}_P = 254\,\text{days}$ |
| | $\sigma = 8\,\text{days}$ | $\sigma = 140\,\text{days}$ |
| LCE diameter | $\text{LCE}_D = 299.8\,\text{km}$ | — |
| | $\sigma = 16.7\,\text{km}$ | — |
| LC northernmost latitude | $\text{LC}_{NL} = 26.88^\circ\,\text{N}$ | $\text{LC}_{NL} = 26.20^\circ\,\text{N}$ |
| | $\sigma = 0.07^\circ\text{N}$ | $\sigma = 0.95^\circ\text{N}$ |
| LC retreat latitude | $\overline{\text{LC}_{RL}} = 24.18^\circ\,\text{N}$ | $\overline{\text{LC}_{RL}} = 25.99^\circ\,\text{N}$ |
| | $\sigma = 0.14^\circ\text{N}$ | $\sigma = 0.78^\circ\text{N}$ |
| Total mean available potential energy | $\langle\text{MAPE}\rangle = 1.80 \times 10^{18}\,\text{J}$ | |
| Total eddy available potential energy | $\langle\text{EAPE}\rangle = 0.97 \times 10^{18}\,\text{J}$ | |
| Total mean kinetic energy | $\langle\text{MKE}\rangle = 2.46 \times 10^{15}\,\text{J}$ | |
| Total eddy kinetic energy | $\langle\text{EKE}\rangle = 2.47 \times 10^{15}\,\text{J}$ | |
| Energy Burger number | $Bu_e = 13.70 \times 10^{-4}$ | |

*Abbreviations:* LC, Loop Current; LCE, Loop Current Eddy.
*Note.* The overline denotes temporal mean and $\sigma$ standard deviation.

The main dynamical features of the upper circulation and energy patterns in the GoM are well reproduced by the model. The good results of the model validation, in conjunction with the model characteristics, suggest that it is adequate for the objectives of this study.

### 3.2. Description of the LCE Shedding Process

For every case study, with the configuration implemented for this study, the LCE shedding process is very regular: the LC penetration and the shedding of the LCEs are quasiperiodic. The spatial distribution pattern of the energy fields is the same, varying only in magnitude, and the trajectories of the LCEs are not significantly affected by changes in either stratification or YC transport. When considering all the case studies, the northernmost and westernmost penetration of the LC is 27.17°N and 89.45°W, respectively, which are somewhat smaller than that observed ones, 28.1°N and 92.7°W (cf. Leben, 2005). The maximum penetration of the LC in the model defines the LC intrusion region represented by the dotted line box in Figure 1b, which in accordance with the model domain, is delimited by [89.59°W, 82.67°W] × [22.04°N, 27.20°N].

In order to analyze the LCE shedding process, a joint dynamical and energetic analysis was carried out considering the LC circulation and the APE. The APE was computed over the LC intrusion region (the dotted box in Figure 1b) and expressed as a density of energy $(\text{J·m}^{-3})$ such that it does not depend on the system size. The time series of the APE density was computed according to the expression $\text{APE}_D(t) = \langle\text{APE}(t)\rangle / \langle H_1(t) + H_2(t)\rangle$.

A very regular behavior of the LCE shedding process is observed in the LC circulation and APE density time series (Figure 4). The typical cycle of the LC circulation exhibits a sustained increase as the LC penetrates the GoM and then a rapid decline to its absolute minimum when a LCE is detached from the LC. The APE density cycle would be similar to that of the LC circulation, but this does not occur. After a sustained increase, the APE density has a relative minimum just when an eddy is about to detach, then it reaches its absolute maximum, and finally, it has a rapid decline to its absolute minimum. This behavior is because, in each eddy detachment event, a recently detached LCE is still present in the LC intrusion region (the computing domain), which explains the lag between the absolute minima in the LC circulation and APE density. The moments of relative minima in the APE density are strongly correlated with those of the
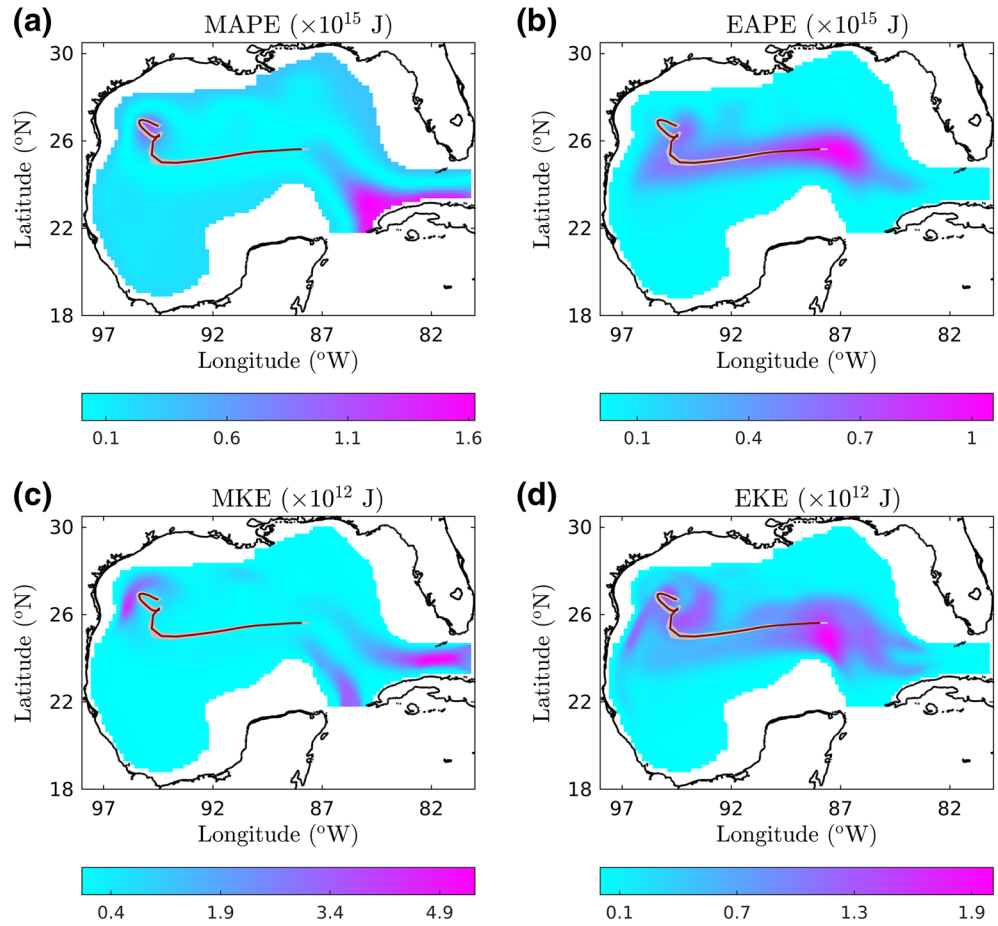
**Figure 3.** Spatial distribution of the mean and eddy energy fields for the base configuration: (a) mean available potential energy MAPE, (b) eddy available potential energy EAPE, (c) mean kinetic energy MKE, and (d) eddy kinetic energy EKE. The individual trajectories (gray lines) and the mean trajectory (red line) of the Loop Current Eddies are also shown.

absolute minima in the LC circulation. However, the correlation is not perfect because the area considered for the computation of the APE density is greater than the area covered by the LC, which introduces small variations. An animation of Figure 4 is included in the supporting information.

From this analysis, it is observed that the LCEs are detached only when the APE density reaches a threshold value, which is different for each GoM configuration. For each APE density threshold value there is an associated $\langle MAPE \rangle$ budget, that is, the $\langle MAPE \rangle$ budget is a condition for the shedding of LCEs. To the knowledge of the authors, there is no observational or numerical evidence of this mechanism. The validation of this mechanism using observations or outputs from an OGCM is beyond the scope of this study.

### 3.3. Effects of Stratification and YC Transport Variations

The relationships between the mean values of the LCS metrics ($\overline{LCE_P}$, $\overline{LCE_d}$, $\overline{LC_{NL}}$, and $\overline{LC_{RL}}$) and the energy metrics ($\langle MAPE \rangle$, $\langle EAPE \rangle$, $\langle MKE \rangle$, $\langle EKE \rangle$, and $Bu_e$) with stratification and YC transport for each of the 49 case studies were analyzed. Due to the model configuration, some of the case studies are numerically unstable; therefore, they were not considered in the analysis. Figure 5 shows the LCS metrics and Figure 6 shows the energy metrics. In Figures 5 and 6, the metrics are presented in color scale, the vertical axis represents the YC transport $\Upsilon$, and the horizontal axis represents the upper layer thickness $\overline{\langle H_1 \rangle}$, with both scaled by their corresponding values for the base configuration $\Upsilon_{ref}$ and $\overline{H_{1(ref)}}$, respectively. Also, the percentage variations of the metrics with respect to the base configuration are represented by contours.
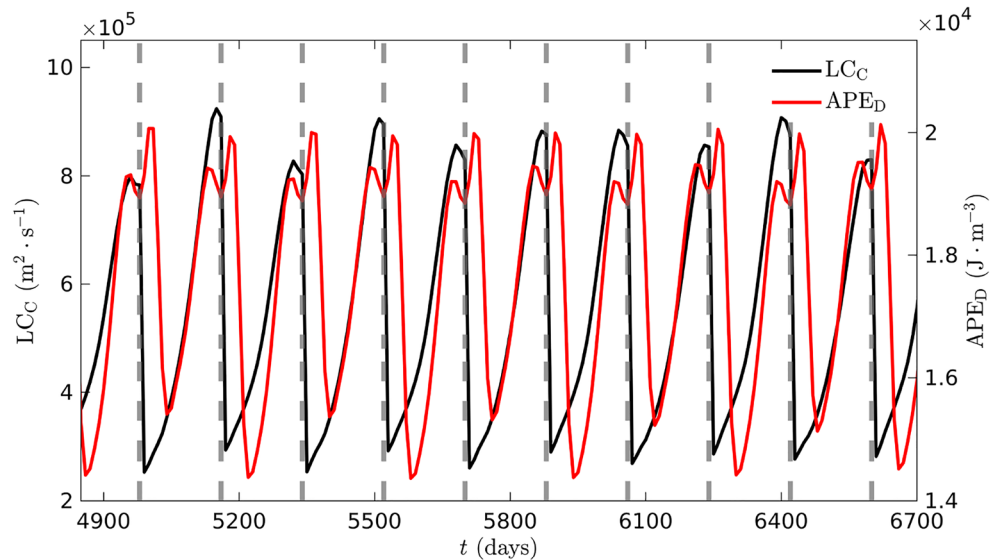
**Figure 4.** Time series of the Loop Current circulation $LC_C$ and the available potential energy density $APE_D$ for the base configuration, computed in the Loop Current intrusion region. Vertical lines indicate the moments when an eddy is about to detach from the Loop Current.

To study the effects of stratification and transport on the LCE shedding process, it is necessary to prove that each case study represents a different state of the LCS with its dynamics, that is, that the mean values of the LCS metrics are statistically different from each other. Tests for differences of mean were performed for $LCE_P$, $LCE_D$, $LC_{NL}$, and $LC_{RL}$, considering each pair-combination of the case studies. The test for differences of mean under independence, with the null hypothesis that the true difference of the mean of two case studies is zero (Wilks, 2011), was used. The testing process rejected the null hypothesis for $\overline{LCE_P}$, $\overline{LCE_d}$, and $\overline{LC_{NL}}$; but failed to reject it for $\overline{LC_{RL}}$ at 5% significance level for most of the pair-combinations. Nevertheless, due to the very regular LCE shedding behavior, for longer simulations the testing process is expected to be corroborated for all the pair-combinations.

From the results of the experiments (Figure 5) it is observed that the same LC retreat latitude is associated with different LCE shedding periods, which would seem to differ from studies using an observational database (cf. Leben, 2005), in which it was found that the greater the LC retreat latitude, the longer the LCE shedding period. The apparent inconsistency between the results of this study with those of Leben (2005) can be explained by noting that the LCE shedding process is associated with a process of increase in the mass of the LC. For each case study, the LC retreat latitude is the same, but the LCE diameter is different. In the results of this work, a bigger LCE diameter is associated with a greater penetration of the LC and a longer LCE shedding period, namely with a greater increase in the mass of the LC. Hence, the LCE diameter depends on the increase in the LC mass, and it is possible to have the same LC retreat latitude but with different LCE shedding periods.

From the process of increase in the LC mass described above, additional details of the LCE shedding process can be deduced. Larger stratification or greater YC transport leads to a greater LC penetration and a bigger LCE diameter, which requires a greater increase in the mass of the LC, and consequently, larger ⟨MAPE⟩ (Figures 5 and 6). Since the LC shed eddies only when the APE density reaches a specific threshold value, the LCE shedding period is directly related to the time it takes for the LC to reach such APE density value after an eddy detachment (Figure 4). Each GoM configuration is associated with specific energy levels in which the episodes of intrusion-retraction of the LC and the shedding of LCEs occur. After the shedding of a LCE, the APE density budget and increment in the LCS metrics needed for a new eddy detachment are higher for the case studies with larger stratification and greater transport, and therefore more time is needed to satisfy those conditions and complete the eddy shedding cycles (Figure 7). The eddy shedding is associated with the maximum APE density variation, or analogously with the APE density difference between
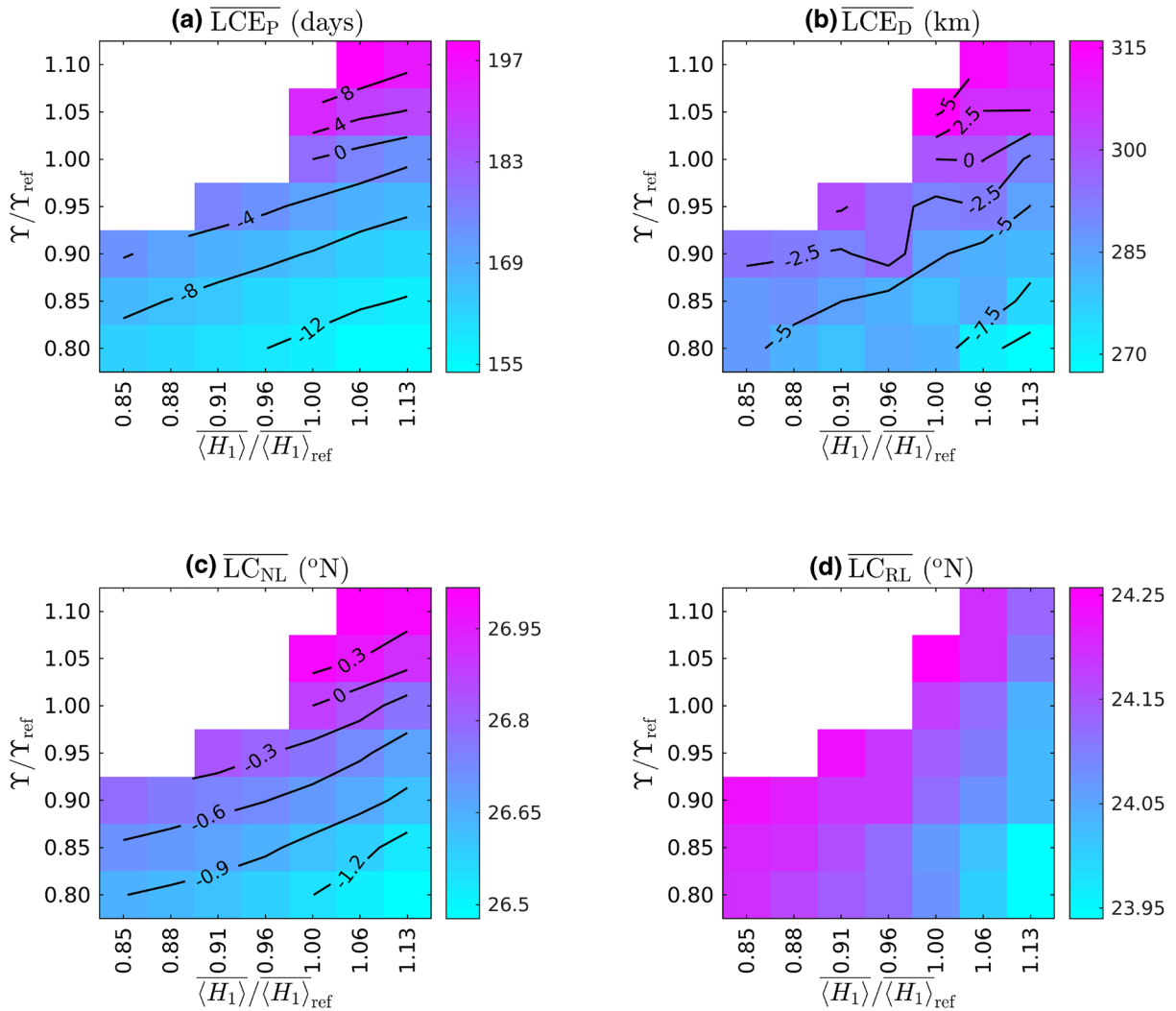
**Figure 5.** Mean values of the LCS metrics ($LCE_P$, $LCE_D$, $LC_{NL}$, and $LC_{RL}$) represented in color scale as a function of the upper layer thickness $\langle H_1 \rangle$ and the YC transport $\Upsilon$, with $\langle H_1 \rangle_{ref} = 76.3$ m and $\Upsilon_{ref} = 22.1$ Sv. Contours represent the percentage variations of the LCS metrics with respect to the base configuration ($\langle H_1 \rangle / \langle H_1 \rangle_{ref} = 1$ and $\Upsilon/\Upsilon_{ref} = 1$). The numerically unstable case studies are shown in blank. LC, Loop Current; LCE, Loop Current Eddy; LCS, Loop Current System; $LCE_P$, LCE shedding period; $LCE_D$, LCE diameter; $LC_{NL}$, LC northernmost latitude; $LC_{RL}$, LC retreat latitude; YC, Yucatan Current.

the retracted and extended states of the LC, rather than the absolute $\langle MAPE \rangle$ content. Nonetheless, the $\langle MAPE \rangle$ content is a direct indicator of this APE density difference. Thus, longer LCE shedding periods are associated with higher $\langle MAPE \rangle$ contents.

Each stratification and YC transport configuration leads to a different dynamics of the LCS (Figures 5 and 6). The LCS metrics, except the LC retreat latitude, and the energy metrics increase as stratification and transport increase. The LCS and energy metrics are more sensitive to transport than to stratification. The energy fields are associated with the velocity in the active layers and the unevenness of the isopycnal surfaces in the following manner (Figures 5 and 6):

- For a fixed stratification, smaller transport is associated with lower input velocities through the Yucatan Channel, producing lower $\langle MKE \rangle$, smaller unevenness of the isopycnal surfaces, and lower $\langle MAPE \rangle$. For larger transport the opposite response is obtained.
- For a fixed YC transport, larger stratification is associated with higher input velocities through the Yucatan Channel, resulting in larger $\langle MKE \rangle$, greater unevenness of the isopycnal surfaces, and larger $\langle MAPE \rangle$. For smaller stratification the opposite response is obtained.
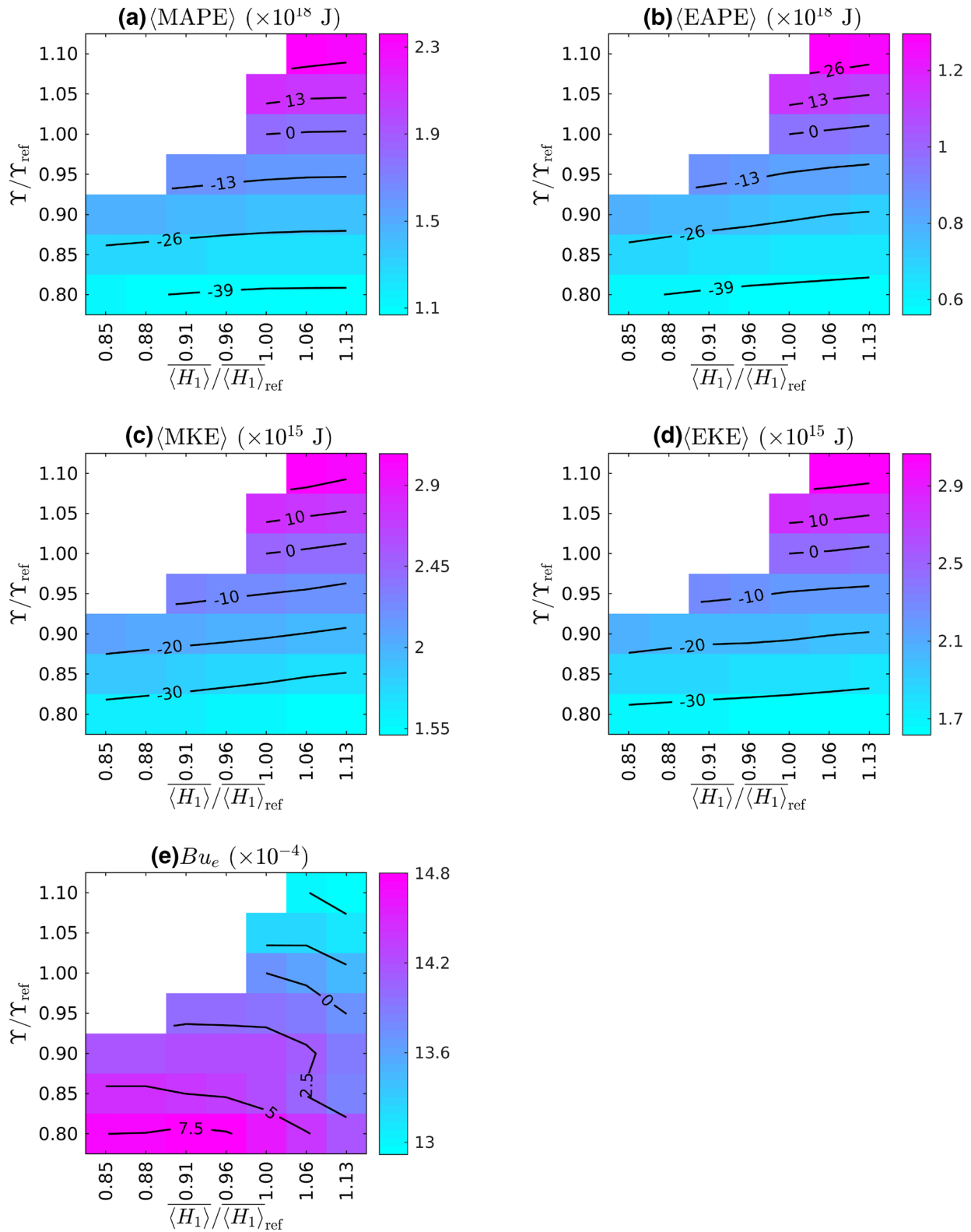
**Figure 6.** Energy metrics ($\langle\text{MAPE}\rangle$, $\langle\text{EAPE}\rangle$, $\langle\text{MKE}\rangle$, $\langle\text{EKE}\rangle$, and $Bu_e$) represented in color scale as a function of the upper layer thickness $\langle H_1 \rangle$ and the YC transport $\Upsilon$, with $\langle H_1 \rangle_{\text{ref}} = 76.3$ m and $\Upsilon_{\text{ref}} = 22.1$ Sv. Contours represent the percentage variations of the energy metrics with respect to the base configuration ($\langle H_1 \rangle / \langle H_1 \rangle_{\text{ref}} = 1$ and $\Upsilon/\Upsilon_{\text{ref}} = 1$). The numerically unstable case studies are shown in blank. $Bu_e$, energy Burger number; EAPE, eddy available potential energy; EKE, eddy kinetic energy; MAPE, mean available potential energy; MKE, the mean kinetic energy.
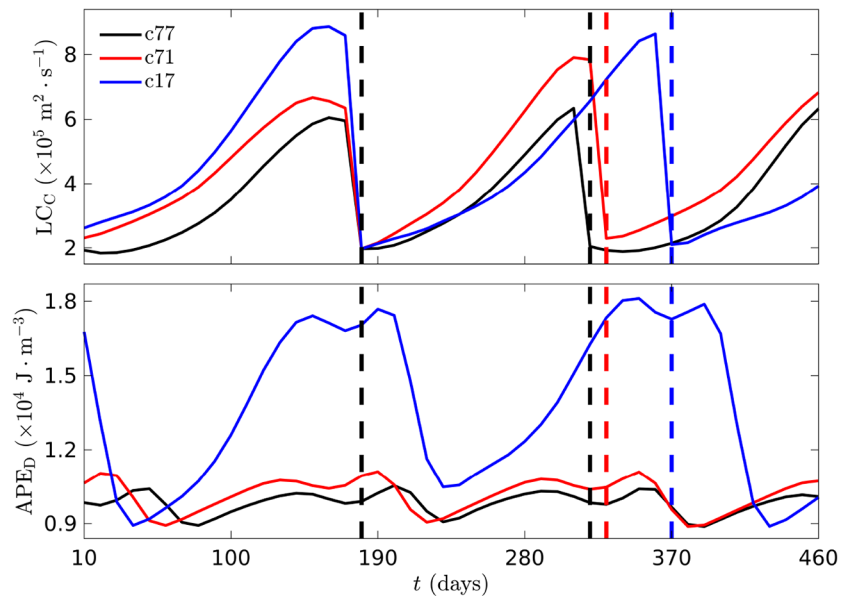
**Figure 7.** Typical cycles of the Loop Current circulation $LC_C$ (top panel) and the available potential energy density $APE_D$ (bottom panel) for a reference case (c77), a larger stratification case (c71), and a greater Yucatan Current transport case (c17). The c71 and c17 series have been shifted in time and downward to make coincident the first eddy detachment at 180 days and have roughly the same minima in all the series. Vertical lines indicate the moments of eddy detachments.

The velocity magnitude in the active layers and the isopycnal surfaces unevenness are greater for transport variations than for stratification variations, resulting in energy metrics more sensitive to transport than to stratification. The mechanism that associates increasing ⟨MAPE⟩ with increasing values of the LCS metrics (Figure 7) indicates that the LCS metrics are more sensitive to transport than to stratification (Figures 5 and 6 and Table 3). The sensitivity to transport is higher for the energy metrics than for the LCS metrics, i.e., for a fixed stratification, variations in transport modify to a great extent the energy metrics; however, these variations have a moderate effect on the choice of the upper layer thickness contour used to compute the LCS metrics. The sensitivity to stratification is similar for the LCS and energy metrics (Figures 5 and 6 and Table 3).

The energy Burger number $Bu_e$ increases as stratification increases, and the YC transport decreases (Figures 5 and 6). $Bu_e$ is the ratio of ⟨MKE⟩ to ⟨MAPE⟩, so its value depends on the relative variations of these two energy fields. Through the case studies, the rate of change of ⟨MAPE⟩ is higher than that of ⟨MKE⟩ (Table 3), resulting in $Bu_e$ mainly determined by the magnitude of ⟨MAPE⟩: generally, high ⟨MAPE⟩ correspond to low $Bu_e$ and vice versa (Figures 5 and 6). The result that ⟨MAPE⟩ dominates $Bu_e$ supports the idea that the dynamics of the LCS is highly related to the content of available potential energy. Nonetheless, it must be remembered that the LCS dynamics involves many different energy transfer processes spanning various temporal and spatial scales (Donohue et al., 2016; Maslo et al., 2020; Yang et al., 2020). Among all those processes, Yang et al. (2020) found that transfer from EAPE to EKE (via buoyancy conversion), and APE transfer from the background flow to mesoscale eddies (via baroclinic instabilities) in the deep eastern GoM basin (deeper than 1,000 m) constitute some of the most important processes in the upper mesoscale energy budget. The main characteristics of such energy transfers are reasonably reproduced by the model used in this study, although it does not reproduce all the energy transfer processes involved in the LCS dynamics.

The results in Figures 5 and 6 and Table 3 show that changes in stratification and YC transport contribute to the observed variability of the LCS reported in the literature (Hall & Leben, 2016; Hamilton et al., 2000; Leben, 2005; Sturges & Leben, 2000; Vukovich, 2012), but they do not explain its entire variability, which comes from many other processes previously mentioned. Particularly, the histogram of the LCE shedding period estimated by Leben (2005) using an observational database shows three primary peaks at six, nine,

**Table 3**
*Maximum Absolute and Percentage Variations of the LCS and Energy Metrics for All the Case Studies, Variable YC Transport With Fixed Stratification, and Variable Stratification With Fixed YC transport*

| Metric | | All the case studies | Variable YC transport | Variable stratification |
|---|---|---|---|---|
| LCE shedding period | $\Delta LCE_P$ | 46 days | 45 days | 12 days |
| | | (30%) | (29%) | (7%) |
| LCE diameter | $\Delta LCE_D$ | 48.7 km | 42.8 km | 19.3 km |
| | | (18%) | (16%) | (7%) |
| LC northernmost | $\Delta LC_{NL}$ | 0.54°N | 0.51°N | 0.18°N |
| latitude | | (2%) | (2%) | (1%) |
| Total mean available | $\Delta \langle MAPE \rangle$ | $1.29 \times 10^{18}$ J | $1.29 \times 10^{18}$ J | $0.08 \times 10^{18}$ J |
| potential energy | | (121%) | (121%) | (5%) |
| Total eddy available | $\Delta \langle EAPE \rangle$ | $0.74 \times 0^{18}$ J | $0.73 \times 10^{18}$ J | $0.08 \times 10^{18}$ J |
| potential energy | | (132%) | (129%) | (11%) |
| Total mean | $\Delta \langle MKE \rangle$ | $1.56 \times 10^{15}$ J | $1.54 \times 10^{15}$ J | $0.14 \times 10^{15}$ J |
| kinetic energy | | (103%) | (100%) | (8%) |
| Total eddy | $\Delta \langle EKE \rangle$ | $1.45 \times 10^{15}$ J | $1.43 \times 10^{15}$ J | $0.11 \times 10^{15}$ J |
| kinetic energy | | (90%) | (88%) | (5%) |
| Energy Burger number | $\Delta Bu_e$ | $1.88 \times 10^{-4}$ | $1.39 \times 10^{-4}$ | $0.62 \times 10^{-4}$ |
| | | (15%) | (11%) | (4%) |

*Abbreviations:* LC, Loop Current; LCE, Loop Current Eddy; YC, Yucatan Current.
*Note.* The percentage variation is with respect to the corresponding minimum value. The overline denotes temporal mean.

and 11 months. The base configuration case of this study reproduces the primary shedding period at six months, with variations of up to 46 days for the remaining case studies, in contrast with the observed variability of 150 days reported by Leben (2005) considering only the primary peaks. With this consideration, the model used in this study accounts for 31% of the observed variability in the LCE shedding period.

### 3.4. Climate Change

In this subsection, the expected variations in the LCE shedding process due to climate change are analyzed, which encompass increased upper stratification and reduced YC transport. The case studies for climate change are those delimited by the dotted line box in Figure 2, with the c35 case corresponding to the base configuration, that is, the current average conditions of the LCS.

The expected variations in the LCE shedding process due to increased stratification and reduced transport are contrary. Larger stratification causes increments in the LCE metrics and energy metrics, except $Bu_e$ that decreases. Smaller transport causes reductions in these metrics, except $Bu_e$ that increases. If both changes occur, the values of these metrics are reduced, except $Bu_e$ that increases (Figures 5 and 6). For a combined occurrence of the changes due to climate change, the $\langle MAPE \rangle$ budget is reduced. Since there is a characteristic $\langle MAPE \rangle$ budget at which the LC shed eddies, climate change would increase the LCE activity, that is, the eddy shedding frequency would increase (Figures 5 and 6). Particularly, reduced YC transport would modify the LCE activity to a greater extent than increased stratification, because the $\langle MAPE \rangle$ budget necessary for an eddy shedding is lower for decrements in transport than for increments in stratification.

This analysis provides a first estimate of the response of the LCS in future climate scenarios. Nevertheless, to accurately estimate the variations in the dynamics of the LCE shedding process due to climate change, better knowledge of the expected changes in stratification and YC transport is required.

### 3.5. Comparison with Previous Theoretical Results

The characteristics of the model used in this study make it a useful tool to investigate theoretical and numerical results obtained with simple models (e.g., Nof, 2005; Pichevin & Nof, 1997; Reid, 1972). In this subsection, a corroboration of the mechanism responsible for the detachment of LCEs proposed by Pichevin and Nof (1997) and Nof (2005) was performed. They used the inviscid shallow-water equations and proposed the zonal momentum conservation of the LC flow as the mechanism responsible for the eddy shedding. Nof (2005) found that the eddy generation period is given by

$$\mathrm{LCE_P} = 2R_\mathrm{f} / C_\mathrm{x},\qquad(8)$$

with

$$R_\mathrm{f} = \left[\frac{768 g'Q}{\beta\pi f^2\alpha(2-\alpha)(1+2\alpha)}\right]^{1/5},\qquad(9)$$

$$C_\mathrm{x} = -\frac{\beta R_\mathrm{f}^2\alpha(2-\alpha)}{24(1-\alpha/2)},\qquad(10)$$

where $R_\mathrm{f}$ is the final eddy radius, $C_x$ is the westward translational speed of the eddy, $Q$ is the steady mass flux of the outflow, $\alpha$ is the relative vorticity nondimensionized by the Coriolis parameter $f$, $g'$ is the reduced gravity, and $\beta$ is the linearized meridional variation of the Coriolis parameter.

Equation 8 expresses a relationship that is in agreement with that found in this work, in which the eddy shedding period increases as the eddy diameter increases. Moreover, for all the case studies analyzed here the LCE trajectories are practically the same, so Equation 8 can be expressed as a linear relationship,

$$\overline{\mathrm{LCE_P}} \propto \overline{\mathrm{LCE_D}}.\qquad(11)$$

It was estimated a linear regression for $\overline{\mathrm{LCE_P}}$ and $\overline{\mathrm{LCE_D}}$, giving a coefficient of determination $R^2 = 0.92$ (Figure 8a), which indicates that the results of this work are consistent with those of Nof (2005).

Regarding the final eddy radius, the comparison was performed in the following way. According to Nof (2005), for each case study with fixed stratification, the final eddy radius $R_\mathrm{f}$ changes only by the steady
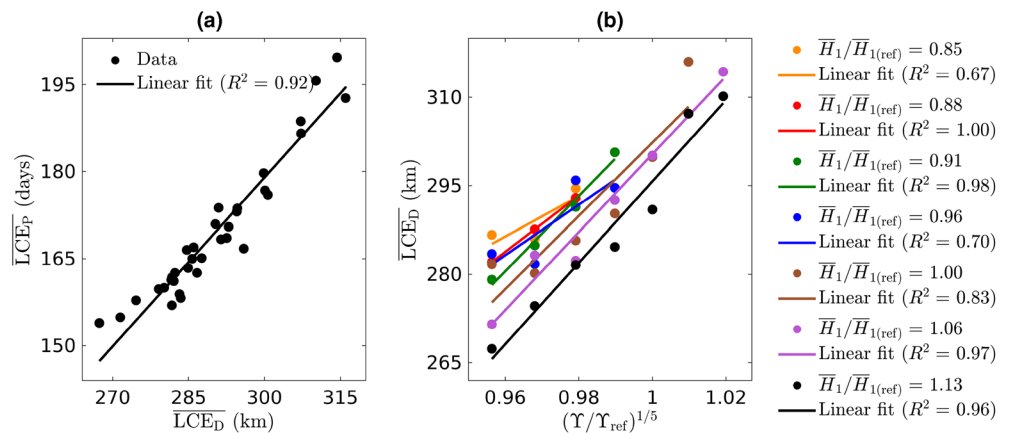


**Figure 8.** (a) Scatter plot of the mean LCE shedding period $\overline{\mathrm{LCE_P}}$ versus the mean LCE diameter $\overline{\mathrm{LCE_D}}$ for all the case studies. (b) Scatter plots of the mean LCE diameter $\overline{\mathrm{LCE_D}}$ versus the YC transport to the one-fifth power $\Upsilon^{1/5}$ for each stratification configuration. For both figures, the corresponding linear fit and coefficient of determination $R^2$ are also shown. LCE, Loop Current Eddy, YC, Yucatan Current.

mass flux of the outflow as $Q^{1/5}$, since the other parameters in Equation 9 do not change. Applied to this study, the Equation 9 expresses a linear relationship between the mean LCE diameter and the YC transport to the one-fifth power,

$$\overline{\mathrm{LCE_D}} \propto \Upsilon^{1/5}. \tag{12}$$

Figure 8b displays scatter plots of $\overline{\mathrm{LCE_D}}$ versus $\Upsilon^{1/5}$ for each stratification configuration, showing an approximately linear relationship between the two variables. Hence, there is a good agreement between the results of Nof (2005) and those of this study.

The model used in this study adds more complexity in modeling the upper GoM hydrodynamics than the model used by Pichevin and Nof (1997) and Nof (2005) (see the model description in Subsection 2.1). The correspondence between the results of Nof (2005) and those of this work supports the idea that the zonal momentum conservation of the LC flow represents one of the fundamental mechanisms for the LCE formation. The particular features of the model allowed achieving the results presented in this work, providing valuable new information about the LCE formation mechanism, which would be tough to obtain by using very complex models, such as OGCMs.

### 3.6. Discussion

This work focused on studying the LCS variability due to upper stratification and upper YC transport, typically above the 500 m depth and the 12.0°C isotherm. The chosen 2½ layered model adequately reproduces the most important dynamical features of the LCS in the upper layer, but with a relatively low variability compared to observations because of the intermediate complexity of the model that does not incorporate all the physical processes that determine its dynamics. Nevertheless, the model fulfills the requirements for this study as it made it possible to explore the causality of a very complex system and answer the posed questions in the study objectives. To a certain extent, the obtained results correspond to the expected LCS behavior, although they do not deliver an entirely realistic representation of its hydrodynamics.

The LCS is a very complex system involving many different phenomena interacting in a highly nonlinear manner. Studies focusing on specific processes, using an adequate model configuration, are particularly useful to obtain an in-depth understanding of the analyzed system. The use of very complex models, such as OGCMs that include all the forcings, would mask the effect of each one, and it would be tough to study their influence separately. By disaggregating the influence of stratification and YC transport, the model used here made it possible to investigate additional characteristics of the LCS and obtain a detailed evaluation of its sensitivity to these processes.

Among all the different phenomena involved in the LCS dynamics, the YC transport is of great significance as found in several studies (Athié et al., 2015; Candela et al., 2019; Chang & Oey, 2012, 2013; Hurlburt & Thompson, 1980, 1982; Lin et al., 2009; Oey et al., 2003; Sheinbaum et al., 2002). From observations, approximately 90% of its total mass transport mainly occurs in the first 500 m depth and roughly above the 12.0°C isotherm (Candela et al., 2019; Rousset & Beal, 2010, 2011; Sheinbaum et al., 2002). Thus, this work studies one of the principal forcings of the LCS, the YC transport, incorporating a significant amount of its variability.

Due to the high LCS variability, it is expected that the separate effects of stratification and YC transport identified in this study are masked in observations and outputs from OGCMs. Nevertheless, these results remain as valid characteristics of the LCS dynamics from a first-order approach since they were obtained with a model that solves the primitive equations. It is worth mentioning the variability associated with deep ocean processes that is not represented by the model, which includes deep flows, bottom instability, deep circulation, and deep eddies. Variability in the LC area associated with deep flows below the 6.0°C isotherm in the Yucatan Channel (Bunge et al., 2002) is missing. The development of bottom instability beneath the LC extending deeper than 2,000 m, as a mechanism contributing to the LCE formation (Chérubin et al., 2005), is also absent. The formation of deep eddies and the connection between the upper and deep energy fields during a LCE detachment (Donohue et al., 2016; Hamilton et al., 2016; Yang et al., 2020) are not represented.

Different studies, using different approaches, have pointed out a range of mechanisms involved in the LCS dynamics (as mentioned throughout the study). The results of this study contribute to the comprehension of the LCS by describing additional characteristics of it and incorporating the finding of the content of available potential energy as a mechanism associated with the LCE shedding process. Nonetheless, the LCS is far from being completely understood, and many questions remain open about it.

## 4. Conclusions

The effects of two key ocean processes, stratification and YC transport, on the LCE shedding process were analyzed. Both processes were studied independently using a primitive equation, 2 1/2 nonhomogeneous layered model, that reproduces the main dynamical features of the upper ocean circulation in the GoM. Additionally, a description of the LCS dynamics under climate change was provided.

Both stratification and YC transport modify the LCS dynamics, with different effects on the LCS and energy metrics. Both metrics are more sensitive to transport than to stratification, and the sensitivity to transport is higher for the energy metrics than for the LCS metrics. The LCE shedding resulted in being associated with a process of increase in the mass of the LC, with the dynamics of the LCS highly related to the content of available potential energy, which is also a condition for the detachment of LCEs. The correspondence between the theoretical results of Nof (2005) and those of this study adds evidence to support the zonal momentum conservation of the LC flow as a fundamental mechanism for the LCE formation.

Under the expected scenarios for climate change (Liu et al., 2012; Rhein et al., 2014), the effects on the LCE dynamics are contrary: larger stratification causes increments in the LCE and energy metrics, except the energy Burger number that decreases; conversely, smaller YC transport causes the opposite response. For a combined occurrence of these changes, a reduction in these metrics is expected, except the energy Burger number that increases, which includes an increased LCE activity.

Variations in stratification and YC transport contribute to the LCS variability, both current and future variability due to climate change. The complex behavior of this system is the result of many interacting phenomena involved in its dynamics; however, the processes identified in this work play an important role in its behavior. The relationships found in this study are worth to be validated and further investigated using observations, more complex models, or OGCMs. It is also worth performing a thorough analysis of the effects of stratification and YC transport on the LCS dynamics considering the implementation of an OGCM and incorporating the expected changes in stratification and transport for specific time horizons.

## Data Availability Statement

Model output can be accessed online (http://metadata.icmyl.unam.mx/handle/20.500.12201/10860).

## References

Athié, G., Candela, J., Ochoa, J., & Sheinbaum, J. (2012). Impact of Caribbean cyclones on the detachment of Loop Current anticyclones. *Journal of Geophysical Research*, *117*, C03018. https://doi.org/10.1029/2011JC007090

Athié, G., Sheinbaum, J., Leben, R., Ochoa, J., Shannon, M. R., & Candela, J. (2015). Interannual variability in the Yucatan Channel flow. *Geophysical Research Letters*, *42*(5), 1496–1503. https://doi.org/10.1002/2014GL062674

Bunge, L., Ochoa, J., Badan, A., Candela, J., & Sheinbaum, J. (2002). Deep flows in the Yucatan Channel and their relation to changes in the Loop Current extension. *Journal of Geophysical Research*, *107*(C12), 261–267. https://doi.org/10.1029/2001JC001256

Candela, J., Ochoa, J., Sheinbaum, J., Lopez, M., Perez-Brunius, P., Tenreiro, M., & Arriaza-Oliveros, L. (2019). The flow through the Gulf of Mexico. *Journal of Physical Oceanography*, *49*(6), 1381–1401. https://doi.org/10.1175/JPO-D-18-0189.1

Candela, J., Sheinbaum, J., Ochoa, J., Badan, A., & Leben, R. (2002). The potential vorticity flux through the Yucatan Channel and the loop current in the Gulf of Mexico. *Geophysical Research Letters*, *29*(22), 161–164. https://doi.org/10.1029/2002GL015587

Candela, J., Tanahara, S., Crepon, M., Barnier, B., & Sheinbaum, J. (2003). Yucatan Channel flow: Observations versus CLIPPER ATL6 and MERCA-TOR PAM models. *Journal of Geophysical Research*, *108*(C12), 3385. https://doi.org/10.1029/2003JC001961

Chang, Y.-L., & Oey, L.-Y. (2010). Why can wind delay the shedding of loop current eddies?. *Journal of Physical Oceanography*, *40*(11), 2481–2495. https://doi.org/10.1175/2010JPO4460.1

Chang, Y.-L., & Oey, L.-Y. (2012). Why does the Loop Current tend to shed more eddies in summer and winter? *Geophysical Research Letters*, *39*(5), L05605. https://doi.org/10.1029/2011GL050773

Chang, Y.-L., & Oey, L.-Y. (2013). Loop current growth and eddy shedding using models and observations: Numerical process experiments and satellite altimetry data. *Journal of Physical Oceanography*, *43*(3), 669–689. https://doi.org/10.1175/JPO-D-12-0139.1

Chérubin, L. M., Sturges, W., & Chassignet, E. P. (2005). Deep flow variability in the vicinity of the Yucatan Straits from a high-resolution numerical simulation. *Journal of Geophysical Research: Oceans*, *110*, C04009. https://doi.org/10.1029/2004JC002280

Colin de Verdière, A., Huck, T., Pogossian, S., & Ollitrault, M. (2018). Available potential energy in density coordinates. *Journal of Physical Oceanography*, *48*(8), 1867–1883. https://doi.org/10.1175/JPO-D-17-0272.1

Damien, P., Pasqueron de Fommervault, O., Sheinbaum, J., Jouanno, J., Camacho- Ibar, V. F., & Duteil, O. (2018). Partitioning of the open waters of the Gulf of Mexico based on the seasonal and interannual variability of chlorophyll concentration. *Journal of Geophysical Research: Oceans*, *123*(4), 2592–2614. https://doi.org/10.1002/2017JC013456

Donohue, K., Watts, D., Hamilton, P., Leben, R., & Kennelly, M. (2016). Loop Current Eddy formation and baroclinic instability. *Dynamics of Atmospheres and Oceans*, *76*, 195–216. https://doi.org/10.1016/j.dynatmoce.2016.01.004

Gill, A., Green, J., & Simmons, A. (1974). Energy partition in the large-scale ocean circulation and the production of mid-ocean eddies. *Deep Sea Research and Oceanographic Abstracts*, *21*(7), 499–528. https://doi.org/10.1016/0011-7471(74)90010-2

Hall, C. A., & Leben, R. R. (2016). Observational evidence of seasonality in the timing of loop current eddy separation. *Dynamics of Atmospheres and Oceans*, *76*, 240–267. https://doi.org/10.1016/j.dynatmoce.2016.06.002

Hamilton, P., Berger, T. J., Singer, J. J., Waddell, E., Churchill, J. H., Leben, R. R., & Sturges, W. (2000). *Desoto Canyon eddy intrusion study, final report, volume II (Technical Report)*. New Orleans, Louisiana: OCS Study MMS 2000-080 U.S. Department of the Interior, Minerals Management Service, Gulf of Mexico OCS Region.

Hamilton, P., Bower, A., Furey, H., Leben, R., & Pérez-Brunius, P. (2019). The loop current: Observations of deep eddies and topographic waves. *Journal of Physical Oceanography*, *49*(6), 1463–1483. https://doi.org/10.1175/JPO-D-18-0213.1

Hamilton, P., Lugo-Fernandez, A., & Sheinbaum, J. (2016). A Loop Current experiment: Field and remote measurements. *Dynamics of Atmospheres and Oceans*, *76*, 156–173. https://doi.org/10.1016/j.dynatmoce.2016.01.005 (The Loop Current Dynamics Experiment).

Hurlburt, H. E., & Thompson, J. D. (1980). A numerical study of loop current intrusions and eddy shedding. *Journal of Physical Oceanography*, *10*(198010), 1611–1651. https://doi.org/10.1175/1520-0485(1980)010$(\$1611:ANSOLC$)\$2.0.CO;2

Hurlburt, H. E., & Thompson, J. D. (1982). The dynamics of the loop current and shed eddies in a numerical model of the Gulf of Mexico. In J. C. Nihoul (Ed.), Hydrodynamics of semi-enclosed seas (Vol. 34, pp. 243–297). Oxford, UK: Elsevier. https://doi.org/10.1016/S0422-9894(08)71247-9

Le Hénaff, M., Kourafalou, V. H., Morel, Y., & Srinivasan, A. (2012). Simulating the dynamics and intensification of cyclonic loop current frontal eddies in the Gulf of Mexico. *Journal of Geophysical Research*, *117*, C02034. https://doi.org/10.1029/2011JC007279

Leben, R. R. (2005). Altimeter-derived loop current metrics. In W. Sturges, & A. Lugo-Fernandez (Eds.), *Circulation in the Gulf of Mexico: Observations and models* (pp. 181–201). Washington, DC: American Geophysical Union. https://doi.org/10.1029/161GM15

Leipper, D. F. (1970). A sequence of current patterns in the Gulf of Mexico. *Journal of Geophysical Research*, *75*(3), 637–657. https://doi.org/10.1029/JC075i003p00637

Lin, Y., Greatbatch, R. J., & Sheng, J. (2009). A model study of the vertically integrated transport variability through the Yucatan Channel: Role of Loop Current evolution and flow compensation around Cuba. *Journal of Geophysical Research*, *114*, C08003. https://doi.org/10.1029/2008JC005199

Liu, Y., Lee, S.-K., Muhling, B. A., Lamkin, J. T., & Enfield, D. B. (2012). Significant reduction of the Loop Current in the 21st century and its impact on the Gulf of Mexico. *Journal of Geophysical Research*, *117*, C05039. https://doi.org/10.1029/2011JC007555

Lorenz, E. N. (1955). Available potential energy and the maintenance of the general circulation. *Tellus*, *7*(2), 157–167. https://doi.org/10.3402/tellusa.v7i2.8796

Maslo, A., Azevedo Correia de Souza, J. M., & Sheinbaum, J. (2020). Energetics of the deep Gulf of Mexico. *Journal of Physical Oceanography*, *50*(6), 1655–1675. https://doi.org/10.1175/JPO-D-19-0308.1

McCreary, J. P., & Lu, P. (1994). Interaction between the subtropical and equatorial ocean circulations: The subtropical cell. *Journal of Physical Oceanography*, *24*(2), 466–497. https://doi.org/10.1175/1520-0485(1994)024(0466:IBTSAE)2.0.C0;2

Murphy, S. J., Hurlburt, H. E., & O'Brien, J. J. (1999). The connectivity of eddy variability in the Caribbean sea, the Gulf of Mexico, and the Atlantic ocean. *Journal of Geophysical Research: Oceans*, *104*(C1), 1431–1453. https://doi.org/10.1029/1998JC900010

NASEM. (2018). National Academies of Sciences, Engineering, and Medicine: Oceans. *Understanding and Predicting the Gulf of Mexico Loop Current: Critical Gaps and Recommendations*. Washington, DC: The National Academies Press. https://doi.org/10.17226/24823

Nencioli, F., Dong, C., Dickey, T., Washburn, L., & McWilliams, J. C. (2010). A vector GeometryBased eddy detection algorithm and its application to a high-resolution numerical model product and high-frequency radar surface velocities in the southern California Bight. *Journal of Atmospheric and Oceanic Technology*, *27*(3), 564–579. https://doi.org/10.1175/2009JTECHO725.1

Niiler, P. P., & Kraus, E. B. (1977). One-dimensional models of the upper ocean. In E. B. Kraus (Ed.), *Modelling and prediction of the upper layers of the ocean* (pp. 143–172). Oxford, UK: Pergamon Press.

Nof, D. (2005). The momentum imbalance paradox revisited. *Journal of Physical Oceanography*, *35*(10), 1928–1939. https://doi.org/10.1175/JPO2772.1

Oey, L.-Y. (2004). Vorticity flux through the Yucatan Channel and loop current variability in the Gulf of Mexico. *Journal of Geophysical Research: Oceans*, *109*, C10004. https://doi.org/10.1029/2004JC002400

Oey, L.-Y., Ezer, T., & Lee, H. (2005). Loop current, rings and related circulation in the Gulf of Mexico: A review of numerical models and future challenges. In W. Sturges, & A. Lugo-Fernandez (Eds.), *Circulation in the Gulf of Mexico: Observations and models* (pp. 31–56). Washington, DC: American Geophysical Union. https://doi.org/10.1029/161GM04

Oey, L.-Y., Lee, H.-C., & Schmitz, W. J. (2003). Effects of winds and Caribbean eddies on the frequency of loop current eddy shedding: A numerical model study. *Journal of Geophysical Research: Oceans*, *108*, 3324. https://doi.org/10.1029/2002JC001698

Oort, A. H., Ascher, S. C., Levitus, S., & Peixóto, J. P. (1989). New estimates of the available potential energy in the world ocean. *Journal of Geophysical Research: Oceans*, *94*(C3), 3187–3200. https://doi.org/10.1029/JC094iC03p03187

Peterson, K. A., & Greatbatch, R. J. (2001). Vorticity fluxes in shallow water ocean models. *Atmosphere-Ocean*, *39*(1), 1–14. https://doi.org/10.1080/07055900.2001.9649662

Pichevin, T., & Nof, D. (1997). The momentum imbalance paradox. *Tellus A*, *49*(2), 298–319. https://doi.org/10.1034/j.1600-0870.1997.t01-1-00009.x

Reid, R. O. (1972). A simple dynamic model of the Loop Current. In L. R. A. Ca- purro, & J. L. Reid (Eds.), *Contributions on the physical oceanography of the Gulf of Mexico* (Vol. 2, pp. 157–159). Gulf Publishing.

Reid, R. O., Elliott, B. A., & Olson, D. B. (1981). Available potential energy: A clarification. *Journal of Physical Oceanography*, *11*(1), 15–29. https://doi.org/10.1175/1520-0485(1981)011$(\$0015:APEAC$)\$2.0.CO;2

Rhein, M., Rintoul, S., Aoki, S., Campos, E., Chambers, D., Feely, R., & Wang, F. (2014). Observations: Ocean. In T. F., Stocker, D. Qin, G.-K. Plattner, M. Tignor, S. K. Allen, J. Boschung, et al. (eds.) *Climate change 2013 the physical science basis: Working group I contribution to the fifth assessment report of the intergovernmental panel on climate change.* (pp. 255–316). Cambridge, UK and New York, NY, USA: Cambridge University Press. https://doi.org/10.1017/CBO9781107415324.010

Rousset, C., & Beal, L. M. (2010). Observations of the Florida and Yucatan currents from a Caribbean cruise ship. *Journal of Physical Oceanography: Oceans*, *40*(7), 1575–1581. https://doi.org/10.1175/2010JPO4447.1

Rousset, C., & Beal, L. M. (2011). On the seasonal variability of the currents in the Straits of Florida and Yucatan Channel. *Journal of Geophysical Research*, *116*, C08004. https://doi.org/10.1029/2010JC006679

Schmitz, W. J. (2005). Cyclones and westward propagation in the shedding of anticyclonic rings from the loop current. In W. Sturges, & A. Lugo-Fernandez (Eds.), *Circulation in the Gulf of Mexico: Observations and models* (pp. 241–261). Washington, DC: American Geophysical Union. https://doi.org/10.1029/161GM18

Schmitz, W. J., Biggs, D. C., Lugo-Fernandez, A., Oey, L.-Y., & Sturges, W. (2005). A synopsis of the circulation in the Gulf of Mexico and on its continental margins. In W. Sturges, & A. Lugo-Fernandez (Eds.), *Circulation in the Gulf of Mexico: Observations and models* (pp. 11–29). Washington, DC: American Geophysical Union. https://doi.org/10.1029/161GM03

Sheinbaum, J., Candela, J., Badan, A., & Ochoa, J. (2002). Flow structure and transport in the Yucatan Channel. *Geophysical Research Letters*, *29*(3), 101–104. https://doi.org/10.1029/2001GL013990

Simonnet, E., Ghil, M., Ide, K., Temam, R., & Wang, S. (2003). Low-frequency variability in shallow-water models of the wind-driven ocean circulation. Part I: Steady-state solution. *Journal of Physical Oceanography*, *33*(4), 712–728. https://doi.org/10.1175/1520-0485(2003)33(712:LVISMO)2.0.CO;2

Sturges, W., & Leben, R. (2000). Frequency of ring separations from the loop current in the Gulf of Mexico: A revised estimate. *Journal of Physical Oceanography*, *30*(7), 1814–1819. https://doi.org/10.1175/1520-0485(2000)030$($1814:FORSFT$)$2.0.CO;2

Vukovich, F. M. (2012). Changes in the loop current's eddy shedding in the period 2001-2010. *International Journal of Oceanography*, *2012*(439042), 1–18. https://doi.org/10.1155/2012/439042

Weisberg, R. H., & Liu, Y. (2017). On the loop current penetration into the Gulf of Mexico. *Journal of Geophysical Research: Oceans*, *122*(12), 9679–9694. https://doi.org/10.1002/2017JC013330

Wilks, D. S. (2011). *Statistical methods in the atmospheric sciences* (Vol. 100, 3rd ed). San Diego, Ca: Academic Press.

Yang, Y., Weisberg, R. H., Liu, Y., & San Liang, X. (2020). Instabilities and multiscale interactions underlying the loop current eddy shedding in the Gulf of Mexico. *Journal of Physical Oceanography*, *50*(5), 1289–1317. https://doi.org/10.1175/JPO-D-19-0202.1

Yoskowitz, D., Leon, C., Gibeaut, J., Lupher, B., Lopez, M., Santos, C., & McKin- ney, L. (2013). *Gulf 360: State of the Gulf of Mexico* (Technical Report). Texas A&M University-Corpus Christi, Texas: Harte Research Institute for Gulf of Mexico Studies.

Zavala-Hidalgo, J. (1997). *Estudio numérico de la circulación y termodinámica estacional del Golfo de México*. (Unpublished doctoral dissertation). Centro de Investigación Científica y de Educación Superior de Ensenada, CICESE.

Zavala-Hidalgo, J., Morey, S. L., & O'Brien, J. J. (2003). Cyclonic eddies northeast of the Campeche bank from altimetry data. *Journal of Physical Oceanography*, *33*(3), 623–629. https://doi.org/10.1175/1520-0485(2003)033(0623:CENOTC)2.0.CO;2

Zavala-Hidalgo, J., Morey, S. L., O'Brien, J. J., & Zamudio, L. (2006). On the Loop Current eddy shedding variability. *Atmosfera*, *19*(1), 41–48.

Zavala-Hidalgo, J., Parés-Sierra, A., & Ochoa, J. (2002). Seasonal variability of the temperature and heat fluxes in the Gulf of Mexico. *Atmósfera*, *15*(2). 81–104.

Zemskova, V. E., White, B. L., & Scotti, A. (2015). Available potential energy and the general circulation: Partitioning wind, buoyancy forcing, and diapycnal mixing. *Journal of Physical Oceanography*, *45*(6), 1510–1531. https://doi.org/10.1175/JPO-D-14-0043.1

Zhao, B., Cheng, L., & Sun, W. (2020). Solitary waves of two-layer quasi-geostrophic flow and analytical solutions with scalar nonlinearity. *Dynamics of Atmospheres and Oceans*, *89*, 101129. https://doi.org/10.1016/j.dynatmoce.2019.101129